CHEMISTRY OF MATERIALS

ARTICLE

pubs.acs.org/cm

Advanced Electrodes for Solid Acid Fuel Cells by Platinum Deposition on CsH_2PO_4

Alexander B. Papandrew,*[‖] Calum R.I. Chisholm,[†] Ramez A. Elgammal,[‡] Mustafa M. Özer,[¶] and Strahinja K. Zecevic[§]

[†]Division of Engineering and Applied Science, California Institute of Technology, Pasadena, California 91125, United States

[‖]Department of Chemical and Biomolecular Engineering and [‡]Department of Chemistry, University of Tennessee, Knoxville, Tennessee 37996, United States

[¶]Materials Science and Technology Division, Oak Ridge National Laboratory, Oak Ridge, Tennessee 37831, United States

[§]LiOx, Inc., Pasadena, California 91106, United States

Supporting Information

ABSTRACT: We demonstrate cathodes for solid acid fuel cells fabricated by vapor deposition of platinum from the metalorganic precursor $Pt(acac)_2$ on the solid acid CsH_2PO_4 at 210 °C. A network of platinum nanoparticles with diameters of 2−4 nm serves as both the oxygen reduction catalyst and the electronic conductor in the electrode. Electrodes with a platinum content of 1.75 mg/cm^2 are more active for oxygen reduction than previously reported electrodes with a platinum content of 7.5 mg/cm^2. Electrodes containing <1.75 mg/cm^2 of platinum show significantly reduced catalytic activity and increased ohmic resistance indicative of a highly discontinuous catalytic-electronic platinum network.

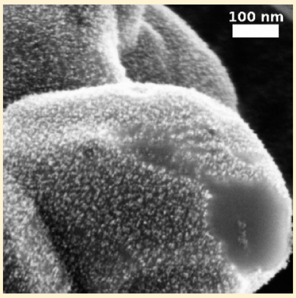

KEYWORDS: catalysis and catalysts, nanomaterials (nanoparticles, nanotubes, etc.), ionic conductors (including solid (inorganic) and polymer electrolytes

INTRODUCTION

Solid acid fuel cells (SAFCs) have made the transition from a laboratory curiosity to a commercially viable energy conversion technology with considerable speed. Although first introduced in 2000,[1] by 2005, an SAFC with a peak power density of 415 mW/cm^2 had been demonstrated.[2] Current SAFCs are based on the solid-state electrolyte CsH_2PO_4 (CDP),[3] which, above 230 °C, undergoes a solid-state phase transformation to a superprotonic phase characterized by a large increase in proton conductivity. At a typical operation temperature of 250 °C, the conductivity of CDP is 2.5×10^{-2} S cm^{-1}. Operation at this temperature imparts a tolerance to fuel stream impurities such as CO and H_2S in amounts of 20% and 100 ppm,[4,5] respectively, largely eliminating the need for cleanup of reformed hydrocarbon reactants. Moreover, methanol vapor may be reformed internally within the membrane-electrode assembly (MEA)[3,6] by the addition of a $CuO/ZnO{:}Al_2O_3$ catalyst layer, obviating the need for an external reformer and greatly simplifying system design. The solid nature of the electrolyte renders the membrane extraordinarily resistant to reactant crossover, and its superplasticity in the superprotonic phase acts to "heal" minor breaches of the membrane in situ.[5] A comprehensive review of the early stages of SAFC development has been presented by Haile et al.[4]

The unique characteristics of the CDP electrolyte pose several challenges to SAFC optimization, particularly in the area of cathode microstructure. Other fuel cell electrolytes (Nafion[7] and similar polymers,[8] phosphoric acid, solid oxide ion conductors) exhibit oxygen permeability, allowing for large active areas that are essentially limited by the surface area of the catalyst. The lack of oxygen solubility in CDP demands that an active site be co-located at the intersection of the electrolyte, catalyst, and pore. Furthermore, there must exist a percolating network of electrolyte and pores, and some combination of catalyst and electronic conductor (e.g., carbon).

The first SAFC cathodes[3] made use of a mechanical mixture of CDP, platinum black, and carbon in empirically derived ratios, compressed to enforce the connectivity of the necessary phases. To improve the performance and reduce the platinum content of SAFC cathodes, a more elegant approach was sought. We hypothesized that, if electrolyte particles could be coated evenly in catalyst material, the available electrochemical surface area could be maximized. Moreover, we expected that the superplasticity and high sinterability of superprotonic solid acids[5,9,10] would allow gently compressed CDP particles to form a highly porous, proton-conducting network, even while decorated with a catalytic and electronically conductive outer layer.

Platinum nanoparticles are routinely deposited on powders for catalyst applications by reduction of platinum precursors dissolved in an aqueous solution.[11] This route is incompatible with CDP, which is water-soluble. Vapor-phase deposition of platinum on divided substrates is much less well understood. Some investigators have demonstrated nanostructured platinum film formation on powders with fluidized-bed chemical

Received: April 23, 2010
Revised: January 11, 2011
Published: March 15, 2011

vapor deposition (CVD) methods.[12−16] However, fluidization of particles with a strong self-affinity (such as CDP) and with submicrometer particle sizes has proven difficult.[15] In addition, the high temperatures required for the decomposition of many CVD precursors[17] threaten to induce the dehydration phase transformation in CDP,[18−20] altering the microstructure of the feedstock particles significantly.

The metalorganic platinum(II)(2,4)-pentanedionate [$Pt(acac)_2$] is an attractive candidate for low-temperature deposition of platinum on CDP. Atomic layer deposition from $Pt(acac)_2$[21] has been performed at temperatures as low as 140 °C,[22] and a reduction of various acetylacetonates using alcohols has been demonstrated[23−25] at temperatures of 180−270 °C. Other investigators have also shown that $Pt(acac)_2$ can be used to deposit platinum on porous metal substrates[26] or on metal oxide powders.[27] The reaction mechanism of $Pt(acac)_2$ with surface sites on alumina[28,29] and silica[30,31] has also been studied extensively. Those studies suggest that both surface hydroxyl groups and metal ions (in the case of alumina) play a role in the adsorption and decomposition of $Pt(acac)_2$. On CDP, we expected the process to be similar to alumina, except that surface hydroxyl groups in CDP will be significantly more acidic, leading to more-facile platinum deposition. In this article, we describe the deposition of platinum on CDP using a $Pt(acac)_2$ precursor in a fixed bed and the subsequent fabrication and testing of SAFC electrodes formed from the coated powders.

EXPERIMENTAL SECTION

Coarse-grained CsH_2PO_4 powder was synthesized as described previously.[3] Cs_2CO_3 (Alfa Aesar, 99.9%) and H_3PO_4 (ACS, 85% w/w aqueous solution) were combined in a molar ratio of 1:2 in aqueous solution and subsequently precipitated in methanol, followed by drying of the collected solid in air at 120 °C. The coarse powder was tumbled in a low-energy ball mill with 2-mm-diameter ZrO_2 spherical milling media in methanol for 15 h. The milled powder was recovered by filtration through a 270-mesh stainless steel screen and washing of the milling media with copious methanol. After allowing the slurry to settle for 24 h, the supernatant methanol was decanted off and replaced with toluene. This slurry was also allowed to settle and the toluene was removed by boiling at 120 °C overnight. The fine CDP powder that resulted from this treatment had an average particle size of ~1 μm and a Brunauer−Emmett−Teller (BET) specific surface area of 2.4 m^2/g, measured by nitrogen adsorption with a Micromeritics Gemini VI 2390 surface area analyzer.

Four 3.7-mL borosilicate glass scintillation vials were filled with 20, 40, 80, and 160 mg of $Pt(acac)_2$ (Alfa Aesar, Pt 48% min, Product No. 10526), respectively. To each of these vials was added 200 mg of fine CsH_2PO_4 (CDP) powder. The sample vials were capped and shaken vigorously by hand until the powder mixture appeared to be a uniform, pale yellow color. The caps of the vials were then removed and the vials transferred to a vacuum oven (VWR 1400E). A separate 3.7-mL vial was then filled with 2.1 mL of deionized (DI) water and placed in the oven far from the vials containing the powders. The oven was evacuated with a rotary vane vacuum pump and purged with dry N_2 three times. The oven was then evacuated again to 0.30 bar, and all valves were sealed. The thermostat was set to 210 °C and heating was started immediately. The temperature and pressure of the oven were monitored with a bimetallic strip and a Bourdon tube, respectively. The chamber reached equilibrium after ~75 min at a temperature of 210 °C and a total pressure of 0.8 bar.

After 15 h at 210 °C, the heater was shut off, the water vapor was evacuated, and the oven was allowed to reach room temperature. The sample powders were removed from the vials by gentle shaking onto waxed weighing paper. The powders were weighed and then passed through a stainless steel screen with a 53-μm wire separation to homogenize the particulates.

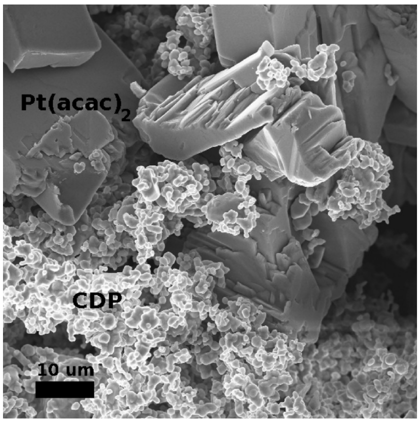

Figure 1. SEM micrograph of a CDP-$Pt(acac)_2$ precursor mixture containing 29 wt % $Pt(acac)_2$ prior to platinum deposition.

Samples of each electrode powder were analyzed by scanning electron microscopy (SEM), energy-dispersive spectrometry (EDS), X-ray photoelectron spectroscopy (XPS), and X-ray diffraction (XRD).

SEM and EDS analyses were performed with a LEO 1525 FESEM system. Images were acquired at an accelerating voltage of 3 kV with the in-lens electron detector, and EDS spectra were acquired at 15 kV with an Oxford INCA detector. Separate CDP-precursor mixtures were also prepared according to the procedure above, and micrographs were recorded at 10 kV to characterize the mixing and contact of CDP and $Pt(acac)_2$.

XPS experiments were carried out in an Omicron ultrahigh vacuum (UHV) chamber with a base pressure better than 5×10^{-11} mbar. The chamber was equipped with a Phi Al Kα X-ray source (10−610E) and monochromator (10−420), and an Omicron electron energy analyzer (EA-125). The samples were affixed to Si crystals (Ted Pella) with a uniaxial pressure of 100 MPa. Before the measurement, the samples were outgassed at ~100 °C, using an indirect heater located underneath the sample holder. In addition to survey scans spanning a wide binding energy range with a step size of 0.5 eV, high-resolution spectra were recorded with a smaller step size for the Pt 4d (0.2 eV), P 2p (0.1 eV), C 1s (0.2 eV), and O 1s (0.1 eV) photoelectron peaks. Adventitious carbon was used to calibrate the binding energy shifts of the sample (C 1s = 284.8 eV).[32] Peak fitting was performed with the XPSPeak[33] software.

XRD analysis was conducted on the as-synthesized samples with a Philips X'Pert X-ray diffractometer, using Cu Kα radiation (λ = 0.15418 nm, 45 kV, 40 mA, 0.05° step, 4.0 s/step). We also examined the solid remnants of powders that had been washed in DI water several times to dissolve the CDP and leave the deposited metal particles intact, obtaining diffraction patterns that were missing the strong CDP peaks. Rietveld refinement was performed on these patterns using the Philips X'Pert Plus software.[34]

Electrodes were formed by spreading the coated powders over an anode-supported half-cell with a total area of 2.85 cm^2 and a CDP membrane thickness of 50 μm, similar to those described elsewhere,[2] followed by compression of the powder at 8 MPa for 3 s. The mass of CDP electrolyte in each electrode was kept constant at 50 mg, and the area-specific platinum loading of the electrodes was 0.88, 1.75, 3.5, and 7 mg/cm^2, respectively. Nickel foam current collectors (INCO) were sealed against each electrode with polytertafluoroethylene (PTFE) tape (McMaster−Carr, Part No. 4591K11) to complete the fabrication of the SAFC MEA.

Each MEA was loaded into a stainless steel test fixture and installed in a test rig. The test fixture was heated to 250 °C and supplied with an

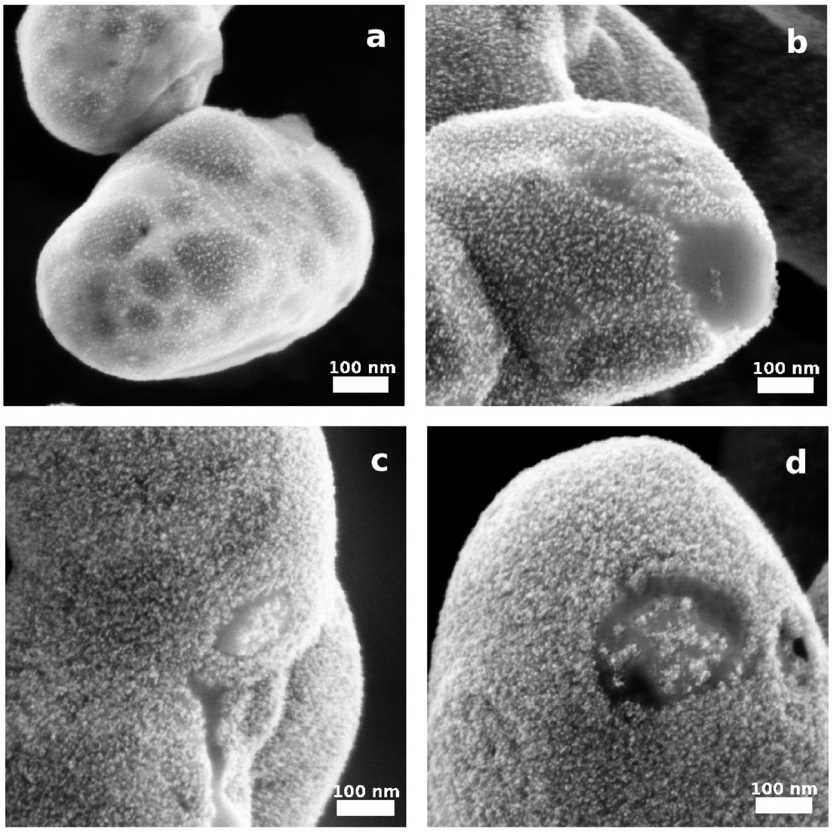

Figure 2. SEM micrograph of (a) 10 mg Pt (5 wt %, 1 nm), (b) 20 mg Pt (9 wt %, 2 nm), (c) 40 mg Pt (17 wt %, 4 nm), and (d) 80 mg Pt (29 wt %, 8 nm), respectively, deposited on 200 mg of CDP powder.

anode reactant flow of 30 sccm of H_2 and a cathode flow of 60 sccm of air. Both reactant streams were hydrated to a dew point of 75 °C. After 12 min of equilibration, a polarization curve was measured with a galvanostat (Keithley 2420) from zero current in increasing steps at a rate of 0.5 s per current step. Up to 200 mA, 200 current steps were distributed according to the function

$$i\,[\mathrm{mA}] = 10^{x/2.3} - 1$$

where the value of x ranges from 0 to 199 in unit steps; thereafter, the current step was 5 mA. The maximum current for the measurement was the current at which the cell voltage was zero. Immediately after the polarization measurement, the ohmic resistance of the cell was measured by the current interrupt technique.[35]

■ RESULTS AND DISCUSSION

An SEM micrograph of a CDP-$Pt(acac)_2$ mixture (29 wt % $Pt(acac)_2$) is shown in Figure 1. The large prismatic $Pt(acac)_2$ crystallites are easily distinguishable from the semispherical agglomerates of CDP.

After thermal treatment, the powders were weighed and each was found to have lost mass equal to the volatile weight fraction of the $Pt(acac)_2$ component (52% of the precursor mass). Identically prepared mixtures powders were treated a second time at 210 °C in vacuum, to check for additional mass loss due to unreacted precursor; none was measured.

High-magnification SEM imaging of the powders after thermal treatment shows no remaining precursor particles and reveals the surface of the CDP particles to be conformally covered with a thin layer of nanoparticles. As the amount of $Pt(acac)_2$ precursor is increased, the thickness of the nanoparticle layer on the CDP qualitatively increases. The change of the surface coverage and morphology of the powders with increasing precursor weight fraction is shown in Figure 2.

Table 1. EDS Measurements of Pt/P and Cs/P Weight Fractions in Pt:CDP Powders.

Pt [wt %]	Pt/P (meas.) $[x_{at}]$[a]	Pt/P (calc.)	Pt/P deviation [%]	Cs/P error [%]
5	0.345 ± 0.052 [0.06]	0.361	−4.4	19.6
9	0.604 ± 0.053 [0.10]	0.722	−16.3	11.0
17	1.450 ± 0.074 [0.24]	1.444	0.4	11.1
29	2.494 ± 0.102 [0.41]	2.888	−13.6	10.5

[a] The measured Pt/P atomic ratio is shown in brackets.

The chemical composition of each powder, as measured by EDS, is composed of the elemental components of CsH_2PO_4 and Pt. Although the strong characteristic P K-peak and the Pt M-peak almost overlap at ~2 kV, we attempted to quantify the platinum content by means of the Pt/P weight ratio. The Pt/Cs ratio, although not confounded by overlapping peaks, was expected to lack accuracy, because of a missing energy calibration standard for Cs on the instrument used. Indeed, the measured ratio of Cs to P deviates by ~10%−20% from the true value of 1:1. Nevertheless, the results in Table 1 show very good agreement for the total amount of platinum, compared to the calculated Pt/P weight ratios based on the platinum content of the precursor. The sampling depth of the EDS technique is ~1 μm, similar to the primary CDP particle size, and it appears that entire particulate volumes have been sampled.

High-resolution XPS scans of the Pt 4d doublet for each sample are presented in Figure 3. The Pt 4d photoelectron peak was chosen, because of the almost overlap of the Cs 4d peaks with the more intense Pt 4f doublet. Three peak components were required to adequately fit the data: these are denoted as peak 1 (solid line), peak 2 (dashed line), and peak 3 (not shown). Peak 3 is a small C 1s loss peak at 313 eV and, for the sake of clarity, is not shown. Peaks 1 and 2 were fit as a doublet with a fixed spin−orbit splitting of 16.9 eV.[36] All peak centers are given in terms of the center of the $4d_{5/2}$ portion of the doublet. Peak 1, at 314.97 ± 0.10 eV, is assigned to platinum metal, in accordance with tabulated data,[37] although the accepted position for the peak is 314.60 eV. Peak 2, at 318.88 ± 0.19 eV, is assigned to the PtO_2, PtO, and/or $Pt(OH)_x$ species, all of which show similar chemical shifts when observed in the Pt 4f peak.[38−41] The positions of the peaks and the ratio of platinum metal to oxide species are listed in Table 2. Platinum oxides are less prevalent at higher platinum loadings. This is most likely due to platinum nuclei already present on the CDP surface acting to catalyze the $Pt(acac)_2$ decomposition reaction, which we discuss in more detail below.

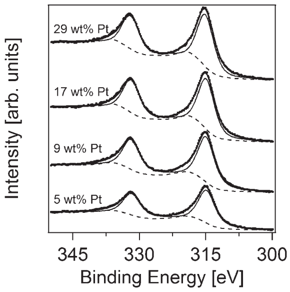

Figure 3. XPS scans of the Pt 4d doublet of Pt:CDP samples. Solid lines are fits to Pt^0 peaks, and dashed lines are fits to Pt oxide/hydroxide peaks. A small C 1s loss peak at 313 eV is omitted in the displayed peaks.

Table 2. XPS Peak Positions and Ratio of Platinum Metal (Pt^0) to Platinum Oxides for Pt:CDP Powders

	Pt $4d_{5/2}$ [eV]		
Pt [wt %]	peak 1	peak 2	Pt/Pt_{oxide}
5	314.87	318.85	6.4
9	314.97	318.81	7.7
17	314.92	318.66	9.1
29	315.1	319.10	9.7

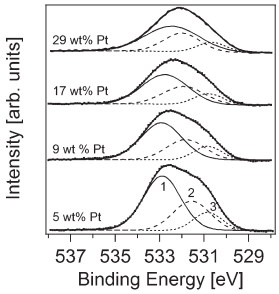

Figure 4. XPS scans of the O 1s peak of Pt:CDP samples. The assignment of peaks 1, 2, and 3 is described in the text.

The interpretation of O 1s photoelectron peaks in the Pt:CDP system is quite complicated. High-resolution scans from the sample powders are presented in Figure 4. Three peak components fit the spectra quite well, but the assignment of these peaks is difficult. The largest of the components, at 532.75 ± 0.24 eV, is likely from nCH_2CH_2O-type species resulting from incomplete ligand decomposition. The peak at 530.76 ± 0.11 eV decreases monotonically with platinum loading, and we can assign it with some confidence to the PO_4 group of the underlying CDP. The peak at 531.815 ± 0.19 eV is likely to contain components from surface hydroxyl groups, PtO, $Pt(OH)_x$, and/or PtO_2. We compared the relative magnitudes of the peaks by normalizing them to the intensity of the most intense peak at 532.75 eV. These results are summarized in Table 3.

C 1s peak scans are presented in Figure 5. In addition to the adventitious peak that has been used as an internal energy reference at 284.8 eV, the C 1s peaks also show evidence of a chemical shift at 287.24 ± 0.14 eV. This peak is assigned most generally to organic fragments from the incomplete decomposition of the $Pt(acac)_2$ precursor. The ratio of adventitious carbon to unknown carbon species is presented in Table 4. There may be evidence for a small autocatalytic effect for decomposition of organic contaminants, but there is no correlation of that effect beyond the lowest platinum loading.

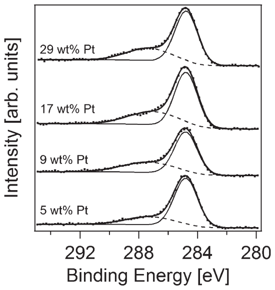

Figure 5. XPS scans of the C 1s peak of Pt:CDP samples. The larger, adventitious carbon peak at 284.8 eV was used as an internal energy standard, and is fit with a solid line. The dashed peak is assigned to organic species resulting from retained organic fragments of the $Pt(acac)_2$ precursor.

Table 3. XPS Peak Positions and Intensities for O 1s Peaks for Pt:CDP Powders

Pt [wt %]	Peak 1 pos. [eV]	Peak 2 pos. [eV]	Peak 2 int.	Peak 3 pos.	Peak 3 int.
5	532.9	531.6	0.51	530.8	0.25
9	532.9	531.8	0.49	530.8	0.25
17	532.8	531.9	0.55	530.8	0.24
29	532.4	532.0	0.51	530.6	0.21
assignment	nCH_2CH_2O	OH, PtO, PtO_2, $Pt(OH)_x$		PO_4	

Table 4. XPS Peak Positions and Ratio of Adventitious Carbon to Unknown Carbon for Pt:CDP Powders

Pt [wt %]	C [eV]	$C_{unknown}$ [eV]	$C/C_{unknown}$
5	284.8	287.26	2.82
9	284.8	287.35	1.80
17	284.8	287.03	1.89
29	284.8	287.30	2.14

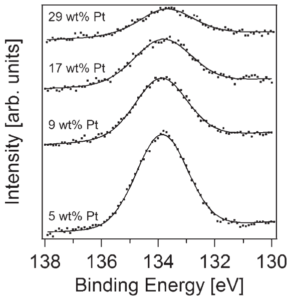

Figure 6. XPS scans of the P 2p peak of Pt:CDP samples and the single fitted peak.

High-resolution scans of the P 2p peaks for the samples are shown in Figure 6. Only one peak component is present at 133.8 ± 0.08 eV, which is expected, given the nature of the ionic bonding in the CDP support. The intensity of the peak decreases with increasing platinum content, because of the combined effect of increasing platinum coverage and the absorption of the emitted P photelectrons by the Pt nanoparticle overlayer.

To estimate the thickening of the Pt nanoparticle layer on the CDP surface, the Pt/P atomic ratio was calculated using the integrated intensities of the Pt $4d_{5/2}$ and P 2p peaks and the associated atomic sensitivity factors. This approach does not explicitly account for the attenuation of the P 2p photoelectrons by the supported Pt nanoparticle layer or the varying coverage of the support at low platinum loadings. The calculated Pt/P atomic ratios for 5, 9, 17, and 29 wt % (bulk) Pt are 1.76, 3.16, 4.25, and 6.27, respectively. These results are significantly increased, with respect to the EDS results in Table 1, because of the extreme surface sensitivity of the XPS technique.

The XPS data show that Pt^0 is the dominant species present in the supported nanoparticles, but that Pt^{II} and/or Pt^{IV} are also likely to be present. Assorted organic species differentiable from adsorbed water and hydrocarbons are also present, although the precise makeup of these compounds cannot be inferred unambiguously. We note that platinum oxides are not deleterious for fuel cell performance, because the oxides are reduced electrochemically during operation. However, high concentrations of organic species may block catalytic sites.

To visually estimate the maximum average thickness of the Pt nanoparticle films, the assumptions of 100% Pt yield and perfect conformal coating were adopted. Based on these assumptions, the thickness of the Pt film is given as

$$t = \frac{1000\phi}{\rho_{Pt}\sigma_{cdp}}$$

Here, t is the film thickness (in nanometers), ϕ the ratio of platinum to CDP mass, ρ_{Pt} the density of platinum (taken to be 21.46 g/cm^3), and σ_{cdp} the specific surface area of the CDP (given in units of m^2/g). Nitrogen adsorption measurements found the specific surface area of the CDP particles discussed here to be 2.4 m^2/g. Therefore, the maximum uniform film thicknesses expected from the experimental samples (10, 20, 40, and 80 mg of platinum per 200 mg of CDP) are 1, 2, 4, and 8 nm, respectively. From inspection of the SEM micrographs, this appears to be a useful model for characterizing the results of the Pt deposition process. Figure 7 shows a powder sample prepared with a platinum loading of 50 wt %, and this is the most illustrative. A cohesive, thick platinum film appears edge-on, and pixel-based measurement of the film thickness with the program ImageJ[42] returned a thickness of 42 ± 3 nm, while the model suggests a film thickness of 53 nm.

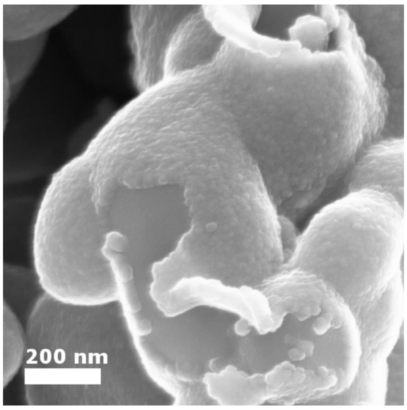

Figure 7. SEM micrograph of 400 mg of Pt (50 wt %, 50 nm) deposited on 200 mg of CDP powder.

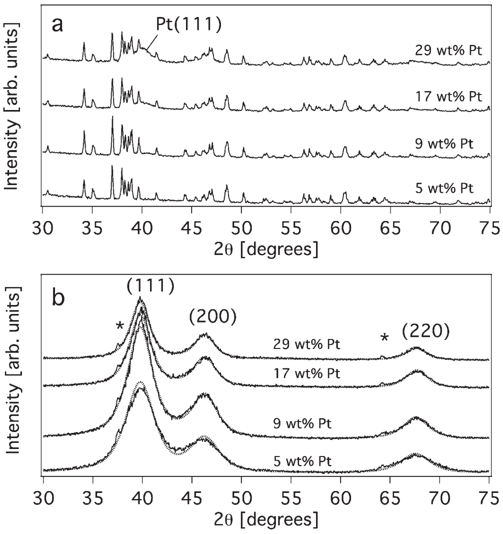

Figure 8. (a) Plot of Cu Kα diffraction patterns from Pt:CDP powders. (b) Diffraction pattern from Pt:CDP powders after CDP removal by washing. Dashed lines are calculated diffraction patterns based on Rietveld refinement. The small peaks marked with a star (★) are remnant CDP peaks.

XRD patterns from the as-coated powders and the washed powders are shown in Figure 8. In the upper portion of the figure, the sharp, highly multiple diffraction peaks of CDP are overlaid on an envelope of broad peaks with the face-centered cubic (fcc) symmetry of platinum. The intensity of the Pt peaks increase with increasing platinum content. In the lower portion of the figure, clear Pt fcc patterns are evident for the washed samples. Rietveld

Table 5. Pt Structural Parameters from XRD

loading [wt% Pt]	lattice parameter [nm]	particle size [nm]
5	0.3916	2.4
9	0.3912	2.8
17	0.3904	3.2
29	0.3910	3.7

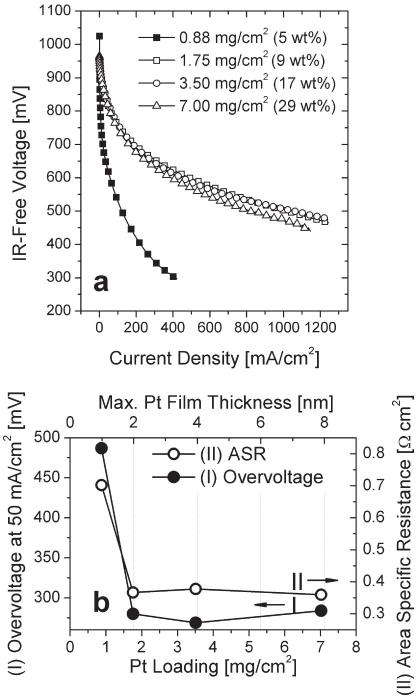

Figure 9. Plot of (a) voltage drop from 1.1 V at 50 mA/cm^2 and (b) ohmic resistance of SAFC electrodes, as a function of platinum loading. Each electrode contained 50 mg of CDP.

refinement of the washed Pt patterns, using the fcc Pt structure,[43] returned, for each sample, a lattice parameter and width of the Pt(111) peak (d-spacing = 0.2265 nm; $2\theta = 39.765°$). Average platinum particle diameters (t) were calculated using the Scherrer equation:

$$t = \frac{0.9\lambda}{B \cos \theta}$$

Here, B is the full width at half maximum (fwhm) intensity of the peak, θ the Bragg angle, and, for Cu Kα_1, $\lambda = 0.154060$ nm. The results are presented in Table 5.

The refined lattice parameters are systematically lower than the value for bulk platinum of 0.39231 nm. Lattice contraction in small metal nanoparticles is a well-known phenomenon and has been observed for platinum,[44] palladium,[45] and other fcc metals.[46] The increase of the average platinum grain size with increased precursor loading is indicative of a nucleation and growth process in which Pt nuclei initially formed on the surface of CDP act to catalyze further Pt reduction and particle growth.

The polarization curves drawn from each of the experimental electrodes, after correction for ohmic resistance, are shown in the upper portion of Figure 9. The large overpotentials are typical of SAFC cathodes,[4,5] which have a paucity of active catalyst sites. Still, the electrode with a Pt surface area of 0.88 mg/cm^2 has a much-higher overvoltage than the electrodes with thicker Pt films. We quantified these overpotentials by measuring the difference between the cell voltage and 1.1 V at a current density of 50 mA/cm^2. The reference voltage was arbitrarily chosen to be approximately equal to the theoretical Nernst potential for H_2/air in the presence of 0.3 atm H_2O at 250 °C, which is 1.12 V for a hydrogen reversible electrode, under these conditions. The measured overpotentials and ohmic resistances are plotted against the platinum loading in the lower portion of Figure 9.

The large increases in overpotential and resistance values at a specific surface area of 0.88 mg/cm^2 are related. At this loading, the average particle size from XRD is 2.4 nm (see Table 5), while the maximum calculated average film thickness is 1 nm. If we discount a preponderance of anisotropic particle shapes, it is clear that complete coverage of the available CDP surface area by platinum is not possible. As the platinum coverage of the CDP network becomes sparse, the electronic path density drops, leading to an attendant increase in the ohmic resistance. Similarly, platinum nanoparticles that are not connected to the electronic conduction network cannot be active catalytically, and the overpotential for the electrode is increased.

Above this critical threshold for complete coverage of the CDP network by platinum, there is no effect of the addition of additional platinum, as shown by the almost-identical activation overvoltages of the remaining samples (see Figure 9). The increase in the platinum particle diameter from 2.8 nm to 3.7 nm with increased loading also has no impact on the oxygen reduction activity of the electrodes, in contrast with the strong dependence of oxygen reduction activity on Pt particle diameter in acidic liquid electrolytes.[47,48] This is clear evidence that it is the electrochemical surface area of the CDP electrolyte, not the Pt catalyst, that dominates the performance of SAFCs. In the case of the highest loading tested, fuel cell performance can be seen to decrease slightly, but at the high current densities indicative of transport losses, rather than kinetic losses. We attribute this effect to an inhibition of proton transport related to constricted particle-to-particle proton conduction pathways in the presence of increasingly thick Pt nanoparticle layers.

Comparisons of the Pt:CDP electrode to the first generation standard SAFC electrodes are favorable. The standard electrode consists of a mechanical mixture of 37.5% platinum black (HiSPEC 1000, Alfa Aesar), 37.5% CDP, 12.5% 0.4Pt on XC-72R (HiSPEC 4000, Alfa Aesar), and 12.5% naphthalene as a fugitive binder/pore former. The electrode weighed 50 mg and had an area-specific platinum loading of 7.5 mg/cm^2. It was formed in the same fashion as the Pt:CDP electrodes, but bonding of the electrode to the membrane proceeded at 120 MPa for 1 min. A representative IR-free polarization curve from the standard electrode is compared to an experimental electrode in Figure 10. The experimental electrode exhibits an overvoltage at 50 mA/cm^2, which is lower by 50 mV and has a voltage in excess of the standard electrode at the higher current densities. Gas diffusion losses are negligible in the Pt:CDP electrode, because of its open structure, as a result of being laminated at 8 MPa. The standard electrode is far more dense and, thus, more acutely affected by gas diffusion losses. A comparison of the two electrode microstructures is shown in Figure 11.

The experimental Pt:CDP electrodes display adequate stability over moderate operation time. An electrode with 1.75 mg/cm^2 of platinum and 50 mg of CDP was operated at a constant current density of 200 mA/cm^2 at 250 °C, with 30/60 sccm H_2/air at a dew point of 75 °C. Over the course of 200 h, the experimental electrode decreased in voltage at a linear rate of

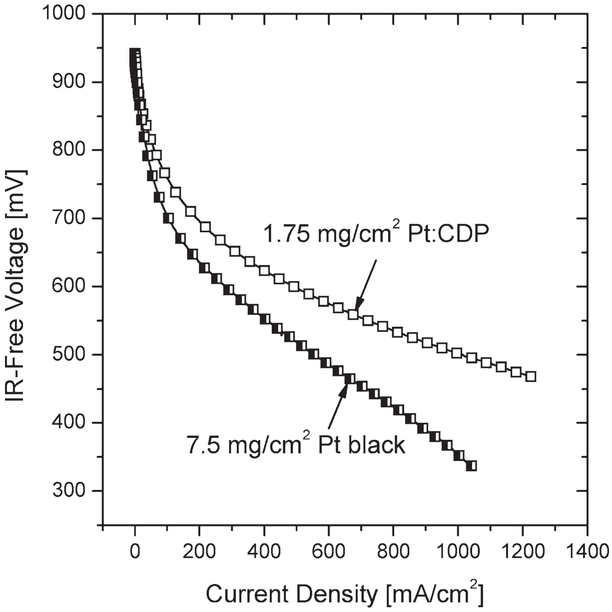

Figure 10. IR-free polarization curves of a standard SAFC electrode and a Pt:CDP electrode.

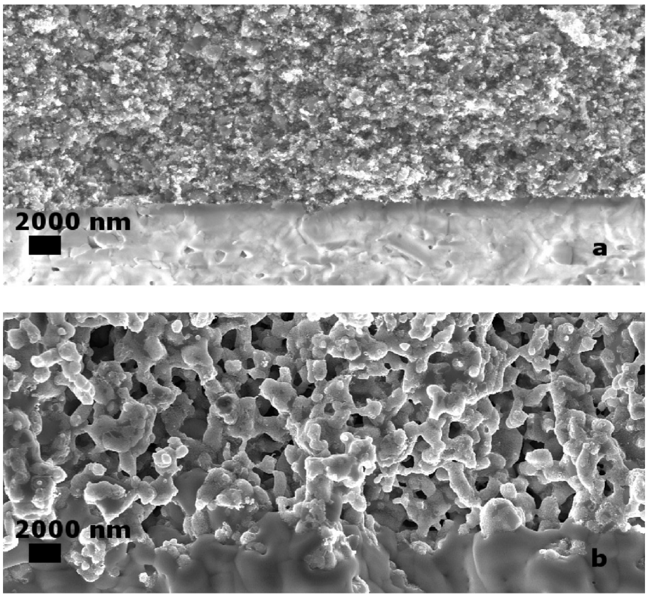

Figure 11. Cross-section electron micrographs of SAFC electrodes: (a) standard SAFC electrode containing Pt black and (b) Pt:CDP electrode.

110 μV/h. Under the same operational conditions, the standard elecrode degrades at the same rate. Voltage decay in SAFCs is a key impediment to commercial adoption and still is not completely understood. We attribute the major modes of voltage loss to changes in the cathode microstructure related to the properties of the CDP electrolyte. CDP is superplastic in its superprotonic phase, leading to large enhancements of the sintering rate of the individual particles in the electrode during fuel cell operation. Sintering closes active catalyst sites to reactant gases, reducing overall catalytic activity and impairing gas diffusion. A concurrent mechanism that has been observed in post-operation SEM studies of Pt:CDP electrodes is a reorganization of the platinum nanoparticles on the surface of the supporting CDP (shown in Figure 12). The high degree of dynamic disorder in the CDP lattice in the superprotonic phase may foster fast diffusion of Pt atoms, leading to a clustering of Pt and eventual disruption of the catalytic-electronic network on the nanoscale. Alternately, platinum may be transported by a vehicle mechanism, because of the formation of small domains of the liquidlike metastable phase of CDP.

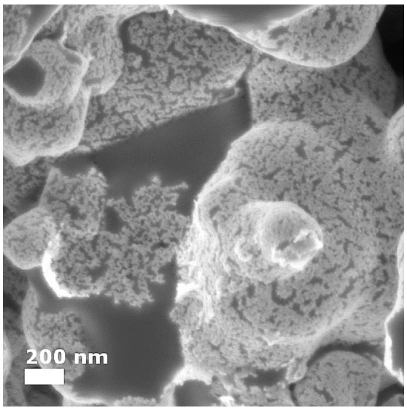

Figure 12. Electron micrograph of a Pt:CDP cathode after fuel cell operation. The bright Pt nanoparticles have reorganized on the darker CDP surface. See text for details.

We are not aware of other methods of platinum deposition that result in the continuous nanoparticle networks that enable the demonstrated electrode advances. The nature of these networks suggest that the surface chemistry of CDP has considerable influence on the deposition process. An infrared spectroscopy study of Pt(acac)$_2$ interactions with surface sites in alumina[29] supports a dissociative mechanism facilitated by surface acidity, and CDP is considerably more acidic than alumina.

In that case, following physisorption of Pt(acac)$_2$ on CDP from the vapor phase, chemisorption will proceed as one acac ligand is dissociated by ligand exchange with surface hydroxyls. The surface of CDP will then contain protonated acac, acacH, and a Pt—O bond. This reaction is thermodynamically favorable and will yield an ionic Pt—O intermediate. The loss of the second acac ligand will then proceed rapidly, yielding a Pt^{II} oxo-type species. Reduction to the dominant Pt^0 species is likely to occur via a two-electron process concomitant with the oxidation of acacH. The minority oxidized Pt species detected by XPS may result from an incomplete reaction or from reaction of Pt^0 with activated surface-bound water. Based on thermogravimetric analysis—mass spectroscopy (TGA-MS) experiments of the decomposition of Pt(acac)$_2$ on related surfaces,[49] acetone, CO, and CH$_4$ are probable byproducts of ligand oxidation. CO may result from decarbonylation of a biacetyl intermediate, as observed in other ligand-mediated reductions of metal centers.[50] It is also possible that radical mechanisms may be occurring under the reaction conditions.[51]

While we cannot rule out an associative mechanism for CDP, in which a phosphate group acts as a nucleophile, followed by the loss of anionic acac, this is not as likely, given the favorable hydrogen-bonding interaction[52] that may exist between the phosphate group and acac ligand and the rather poor nucleophilicity of phosphate (as opposed to phosphines).

Beyond its primary role in preventing the dehydration phase transformation in CDP[3,20] during the deposition process, water may have ancillary effects on Pt deposition. First, water vapor may decrease the activation energy required for deposition, as was observed in related surface-mediated processes.[51] The transition state will involve a structure that has a formation of a Pt^{II}-surface bond and that transition state may be stabilized by hydrogen bonding with water. The presence of water in the chamber may also assist the protonation of the acac ligand to form neutral acetylacetonate, which will be adsorbed on CDP. As CDP has acidic sites, this may only be a secondary consideration. Water may also occupy surface sites to restrict diffusion of Pt atoms, giving a higher density of nucleation and a smaller average crystallite size.

The hypothesized role of the substrate surface suggests much broader catalysis applications of this technique. Carbon, silica, and alumina are workhorse catalyst supports with acidic surfaces and copious adsorbed water. Success in applying our technique to these supports seems likely and offers single-stage processing, fine control over the metal loading, and very high precursor yield. Moreover, the continuous Pt films formed by the addition of larger amounts of precursor suggest the facile synthesis of novel core−shell nanoparticle structures.

The demonstrated coating of the available electrolyte surface area has profound implications for further development of SAFC technologies, using the reported technique. To increase the cathode activity and decrease the significant oxygen reduction overpotential, a higher density of active triple points must be created. The most direct way to achieve this aim is to decrease the average particle size of the CDP in the electrode. As a consequence, the surface area of the electrolyte particles must increase. Of course, following our development above, this would necessitate a corresponding increase in platinum loading for adequate surface coverage and catalytic activity. However, for an electrolyte with a relatively low proton conductivity, such as CDP, the reaction zone for oxygen reduction is highly biased toward the interface with the membrane. It is thus possible that platinum loading may be dropped significantly by the incorporation of a substantially thinner, highly nanostructured electrode.

CONCLUSIONS

We have demonstrated a unique process for depositing platinum on the solid acid CsH_2PO_4 by means of sublimation and decomposition of the metalorganic $Pt(acac)_2$. Platinum nanoparticle networks of varying thickness and coverage were grown on fine CDP powders, and the resultant powders formed into cathodes for solid acid fuel cells (SAFCs) operating at 250 °C. The platinum in these electrodes acts as both the oxygen reduction catalyst and the electronic conductor. Films as thin as 2 nm are sufficient for good electrode activity and resistivity. The addition of more platinum does not improve either property, because the performance of SAFC electrodes is dominated by the electrolyte surface area. Films with a nominal thickness of <2 nm are not sufficient to form a percolating platinum network, and these show substantially decreased activity and increased ohmic resistance. This has important implications for increasing the performance and further reducing the noble metal cost of SAFCs.

ASSOCIATED CONTENT

Supporting Information. Temperature and pressure of vacuum oven before equilibrium during Pt deposition on CsH_2PO_4. (PDF) This material is available free of charge via the Internet at http://pubs.acs.org.

AUTHOR INFORMATION

Corresponding Author

*E-mail: apapandrew@utk.edu.

ACKNOWLEDGMENT

The authors thank Mandy Abbott, Dane Boysen, Suk Yal Cha, Matt Hettermann, and Sossina Haile for technical assistance and helpful discussions. A.B.P. gratefully acknowledges the use of the Caltech GPS Analytical facility and the assistance of Chi Ma, and he also thanks Hanno H. Weitering for the use of his facilities for XPS measurements.

REFERENCES

(1) Boysen, D.; Chisholm, C.; Haile, S.; Narayanan, S. R. *J. Electrochem. Soc.* **2000**, *147*, 3610.
(2) Uda, T.; Haile, S. *Electrochem. Solid-State Lett.* **2005**, *8*, A245.
(3) Boysen, D.; Uda, T.; Chisholm, C.; Haile, S. *Science* **2004**, *303*, 68.
(4) Haile, S.; Chisholm, C.; Sasaki, K.; Boysen, D.; Uda, T. *Faraday Discuss.* **2007**, *134*, 17.
(5) Chisholm, C.; Boysen, D.; Papandrew, A. B.; Zecevic, S.; Cha, S.; Sasaki, K. A.; Varga, A; Giapis, K. P.; Haile, S. M. *Electrochem. Soc. Interface* **2009**, *18*, 53–59.
(6) Uda, T.; Boysen, D.; Chisholm, C.; Haile, S. *Electrochem. Solid-State Lett.* **2006**, *9*, A261.
(7) Gode, P.; Lindbergh, G.; Sundholm, G. *J. Electroanal. Chem.* **2002**, *518*, 115–122.
(8) Zhang, L.; Ma, C.; Mukerjee, S. *Electrochim. Acta* **2003**, *48*, 1845–1859.
(9) Haile, S.; Boysen, D.; Chisholm, C.; Merle, R. B. *Nature* **2001**, *410*, 910–913.
(10) Uda, T.; Boysen, D.; Haile, S. *Solid State Ionics* **2005**, *176*, 127–133.
(11) Spenadel, L.; Boudart, M. *J. Phys. Chem.* **1960**, *64*, 204–207.
(12) Hierso, J.-C.; Serp, P.; Feurer, R.; Kalck, P. *Appl. Organomet. Chem.* **1998**, *12*, 161–172.
(13) Hierso, J.-C.; Feurer, R.; Kalck, P. *Chem. Mater.* **2000**, *12*, 390–399.
(14) Barison, S.; Fabrizio, M.; Carta, G.; Rossetto, G.; Zanella, P. *Thin Solid Films* **2002**, *405*, 81–86.
(15) Vahlas, C.; Juarez, F.; Feurer, R.; Serp, P.; Caussat, B. *Chem. Vap. Deposition* **2002**, *8*, 127–144.
(16) Xu, C.; Zhu, J. *Nanotechnology* **2004**, *15*, 1671–1681.
(17) Thurier, C.; Doppelt, P. *Coord. Chem. Rev.* **2008**, *252*, 155–169.
(18) Taninouchi, Y.-k.; Uda, T.; Awakura, Y.; Ikeda, A.; Haile, S. *J. Mater. Chem.* **2007**, *17*, 3182.
(19) Baranov, A. I.; Kopnin, E. M.; Grebenev, V. V.; Sin, A.; Dubitsky, Y.; Caracino, P. *Phys. Status Solidi A* **2009**, *206*, 36–41.
(20) Taninouchi, Y.-k.; Hatada, N.; Uda, T.; Awakura, Y. *J. Electrochem. Soc.* **2009**, *156*, B572.
(21) Utriainen, M.; Kröger-Laukkanena, M.; Johansson, L.-S.; Niinistö, L. *Appl. Surf. Sci.* **2000**, *157*, 151–158.
(22) Hämäläinen, J.; Munnik, F.; Ritala, M.; Leskelä, M. *Chem. Mater.* **2008**, *20*, 6840–6846.
(23) Premkumar, P.; Bahlawane, N.; Reiss, G.; Kohse-Höinghaus, K. *Chem. Vap. Deposition* **2007**, *13*, 227–231.
(24) Bahlawane, N.; Premkumar, P.; Onwuka, K.; Reiss, G.; Kohse-Höinghaus, K. *Microelectron. Eng.* **2007**, *84*, 2481–2485.
(25) Bahlawane, N.; Premkumar, P. A.; Onwuka, K.; Rott, K.; Reiss, G.; Kohse-Höinghaus, K. *Surf. Coat. Technol.* **2007**, *201*, 8914–8918.

(26) Christoglou, C.; Alphonse, P.; Armand, C.; Desnoyer, C.; Vahlas, C. *Surf. Coat. Technol.* **2007**, *201*, 9195–9199.

(27) Dossi, C.; Pozzi, A.; Recchia, S.; Fusi, A.; Psaro, R. *J. Mol. Catal. A: Chem.* **2003**, *204*—*205*, 465–472.

(28) Womes, M.; Lynch, J.; Bazin, D.; Peltier, F. L.; Morin, S.; Didillon, B. *Catal. Lett.* **2003**, *85*, 25–31.

(29) Womes, M.; Cholley, T.; Peltier, F.; Morin, S.; Didillon, B.; Szydlowski-Schildknecht, N. *Appl. Catal., A* **2005**, *283*, 9–22.

(30) Garcia, J. R. V.; Goto, T. *Mater. Trans.* **2003**, *44*, 1717–1728.

(31) Serp, P.; Kalck, P.; Feurer, R. *Chem. Rev.* **2002**, *102*, 3085–128.

(32) Moulder, F.; Stickle, W.; Solbol, P.; Bomben, K. *Handbook of X-ray Photoelectron Spectroscopy*; Perkin—Elmer Corp.: Eden Prairie, MN, 1992.

(33) Kwok, R. W. M. *XPSPeak*, 1999.

(34) Philips Analytical B.V. *Philips X'Pert Plus*, 1999.

(35) Chisholm, C. R. I.; Boysen, D. A.; Hettermann, M. L.; Papandrew, A. B. U.S. Patent 7,577,536, 2009.

(36) Zsoldos, Z.; Hoffer, T.; Guczi, L. *J. Phys. Chem.* **1991**, *95*, 798–801.

(37) National Institute of Standards and Technology, NIST X-ray Photoelectron Spectroscopy Database, Version 3.5, 2003 (http://srdata.nist.gov/xps/).

(38) Shukla, A.; Neergat, M.; Bera, P.; Jayaram, V.; Hegde, M. S. *J. Electroanal. Chem.* **2001**, *504*, 111–119.

(39) Hamnett, A.; Weeks, S. A. *Electrochim. Acta* **1987**, *32*, 1233–1238.

(40) Allen, G.; Tucker, P.; Capon, A.; Parsons, R. *J. Electroanal. Chem.* **1974**, *50*, 335–343.

(41) Blackstock, J.; Stewart, D.; Li, Z. *Appl. Phys. A: Mater. Sci. Process.* **2005**, *80*, 1343–1353.

(42) Rasband, W. S. *ImageJ* (http://rsb.info.nih.gov/ij/).

(43) Swanson, H.; Tatge, E. *Nat. Bur. Stand. (U.S.), Circular* **1953**, *539*, 1.

(44) Klimenkov, M.; Nepijko, S.; Kuhlenbeck, H.; Bäumer, M.; Schlögl, R.; Freund, H.-J. *Surf. Sci.* **1997**, *391*, 27–36.

(45) Lamber, R.; Wetjen, S.; Jaeger, N. *Phys. Rev. B* **1995**, *51*, 10968–10971.

(46) Montano, P.; Shenoy, G.; Alp, E.; Schulze, W.; Urban, J. *Phys. Rev. Lett.* **1986**, *56*, 2076–2079.

(47) Mukerjee, S.; McBreen, J. *J. Electroanal. Chem.* **1998**, *448*, 163–171.

(48) Mayrhofer, K. J. J.; Blizanac, B. B.; Arenz, M.; Stamenkovic, V. R.; Ross, P. N.; Markovic, N. M. *J. Phys. Chem. B* **2005**, *109*, 14433–14440.

(49) Radivojevic, D.; Seshan, K.; Lefferts, L. *Appl. Catal., A* **2006**, *301*, 51–58.

(50) Harpeness, R.; Gedanken, A. *J. Mater. Chem.* **2005**, *15*, 698.

(51) Battiston, G. A.; Gerbasi, R.; Rodriguez, A. *Chem. Vap. Deposition* **2005**, *11*, 130–135.

(52) Arndt, J.; Klippe, L.; Stolle, R.; Wahl, G. *J. Phys. IV* **1995**, *05*, C5-119–C5-126.